Improved InGaN LED System Efficacy and Cost via Droop Reduction

Final Technical Report

Federal Agency	U.S. Department of Energy
FOA	Solid-State Lighting Advanced Technology R&D DE-FOA-0001171
Award Number	DE-EE0007136
Award Type	Cooperative Agreement
Project Title	Improved InGaN LED System Efficacy and Cost via Droop Reduction
Report	Final Technical Report
Report Number	DOE-LL-0007136-3
Report Period Covered	September 1, 2015 – August 31, 2017
Prime Recipient	Lumileds LLC 370 West Trimble Road San Jose, CA 95131
Principal Investigator	Dr. Isaac Wildeson isaac.wildeson@lumileds.com 408-964-2623

1. Executive summary

Efficiency droop is a non-thermal process intrinsic to indium gallium nitride light emitting diodes (LEDs) in which the external quantum efficiency (EQE) decreases with increasing drive current density. Mitigating droop would allow one to reduce the size of LEDs driven at a given current or to drive LEDs of given size at higher current while maintaining high efficiencies. In other words, droop mitigation can lead to significant gains in light output per dollar and/or light output per watt of input power. This project set an EQE improvement goal at high drive current density which was to be attained by improving the LED active region design and growth process following a droop mitigation strategy. The interactions between LED active region design parameters and efficiency droop were studied by modeling and experiments. The crystal defects that tend to form in more complex LED designs intended to mitigate droop were studied with advanced characterization methods that provided insight into the structural and electronic properties of the material. This insight was applied to improve the epitaxy process both in terms of active region design and optimization of growth parameters. The final project goals were achieved on schedule and an epitaxy process leading to LEDs with EQE exceeding the project target was demonstrated.

2. Objective and accomplishments

2.1. Objective

The overall goal of this project was to substantially improve high current efficiency of InGaN LEDs. Device structures that reduce droop are generally accompanied by significantly increased defect densities – the goal of our project was to use advanced material characterization techniques to understand the source of these defects and how they are affected by the epitaxial growth conditions. Identifying and eliminating defects by improving the epitaxy process will then afford more flexibility in LED device design, enabling devices for high current efficiency improvement. By flattening out the LED EQE curve through Shockley-Read-Hall (SRH) recombination reduction at low current, and droop reduction at high current, LED lighting system design engineers will then have more flexibility in LED system design, enabling LED adoption in a broader array of lighting applications. Critical success factors to achieving this goal were:

- The ability to measure the changes in atomic scale structure that correspond to changes in epitaxial structure and growth conditions
- Correlation of active region structure and growth conditions with the densities and spectroscopic signatures of electronic defects measured by deep-level optical spectroscopy (DLOS)
- The ability to change the metal-organic chemical vapor deposition (MOCVD) process conditions in a way that reduces these defects and the corresponding drop in efficiency
- Theoretical understanding of how carrier transport and droop may be improved by the appropriate LED active region design
- Submitting the most promising improved epitaxy process(es) through a production qualification procedure that ensures requirements for high-volume manufacturing will be satisfied, including yield and reliability requirements.

The project EQE performance goals are defined at high current density and high temperature conditions that are relevant for actual illumination product operating conditions ($100A/cm^2$ | T_j=85°C), measured in a $1mm^2$ or $2mm^2$ commercial flip-chip LED with $\lambda_{typical}$ =442.5nm.

While not a primary goal of the project, green InGaN LED technology also benefited significantly from the knowledge gained throughout this project. The technological challenges for green and blue LEDs are similar and fundamental learning gained from research on one application wavelength is to an extent applicable to the other wavelength.

2.2. Summary of accomplishments

Relative to the objectives above, the following key accomplishments were made.

- Qualitative agreement was shown between computer simulation results for droop-mitigating active region designs and EQE measurements of actual devices incorporating improved designs identified by simulations.
- The same three types of electronic defects identified in DLOS were present in all Lumileds samples studied despite including a wide range of growth conditions and device designs in the sample set. No new type of electronic defect emerged in devices with poor material quality inferred from EQE measurements.
- Defect densities determined by DLOS and lighted capacitance-voltage measurements showed good qualitative agreement with EQE data when the LED active regions being compared had similar layer thickness and number of layers. Correlation of DLOS and EQE results allowed the tentative assignment of one particular electronic level as being primarily responsible for SRH recombination.
- Well-width fluctuations were the only type of *structural* or *extended* defect that showed differences in different LED samples in transmission electron microscopy. Sample-to-sample differences depended on active region design parameters as well as growth conditions. The extent of well-width fluctuations did not have a clear correlation with EQE.
- Combined analysis of DLOS, EQE, and structural characterization results suggested that the main SRH recombination centers in the evaluated LEDs are in fact isolated point defects not associated with structural features visible in advanced electron microscopy.
- It was shown that the time dependence of the cathodoluminescence signal from the quantum wells may give new insight into the electric fields in the active region and effective carrier confinement by the barriers.
- EQE gains hitting the project target were realized in an epitaxy process that completed manufacturing qualification in Q4 2017 ($100A/cm^2$, 442.5nm, T_j=85°C). Gains exceeding the project target have been demonstrated in a further improved process.
- An improved green (530nm) LED epitaxy process was developed that leveraged learning from this project and applied a similar approach. This development resulted in 20% EQE improvement for products scheduled for market release in Q4 2017.

2.3. Milestone summary

A summary of the milestones and completion status is given in Table 1. All applicable milestones were completed and met or exceeded the target performance. While the final project milestones were completed on schedule, some delays were incurred in Year 1 due to negotiation of subaward agreements which delayed the start of work by subrecipients. As discussed below, some milestones were completed with a change in scope vs. the original proposal because the actual outcome of

experiments differed from assumptions that were made when writing the proposal.

Table 1: Milestone summary table (continued on next page).

Task #	Task Title or Subtask Title	Milestone Number	Milestone Description	Milestone Verification Process	Milestone Date	Status
1	Identification of defects within baseline structures					
1.1	Coarse measurement of defects	1.1.1	Establish dependence of defect incorporation on material composition (DLOS)	DLOS(-LCV) deep-level energy assignment, trap density	M2	Completed M6
		1.1.2	Atomic structure characterization on 4-6 samples	Task completion on schedule	M2	Completed M6
1.2	In-depth characterization of initial sample set	1.2.1	Advanced microscopy on 2-3 samples	Task completion on schedule	M6	Completed M9
		1.2.2	Identify atomistic source of SRH defects emergent with different active region structure and growth conditions	DLOS deep-level energy assignment; correlation to growth	M6	Completed with change of scope M9[a)]
1.3	First iterations of epitaxial growth development	1.3.1	Devices showing improvement in material quality (5% EQE gain @ J=0.5A/cm^2)	NIST calibrated efficacy measurement at T_j=85°C	M6	Completed M9
1.4	First evaluation of improved droop epi concepts	1.4.1	Demonstrate at least two device designs that show droop improvement	NIST calibrated efficacy measurement at T_j=85°C	M6	Completed M9
2	Correlate defects to growth conditions; determine atomistic source of defects; Year 1 target EQE gain over baseline at 100A/cm^2, 85°C					
2.1	Coarse measurement of samples grown using latest MOCVD conditions	2.1.1	Identify emergent/ascendant deep level defects within low droop structures	DLOS(-LCV) deep-level energy assignment, trap density; STEM(-EELS) analysis	M8	Completed with change of scope M10[a)]

2.2	Correlate emergent defects to changes in growth conditions	2.2.1	Identify atomistic source of DLOS deep levels	DLOS spectroscopic data and deep-level energy assignment	M12	Completed with change of scope M13[a)]
		2.2.2	Quantify changes in atomic structure and correlate to growth conditions	STEM/3D-APT image and analytical technique analysis	M12	Completed with change of scope M13[a)]
2.4	Evaluation of updated growth conditions in complex LED device designs	2.4.1	Year 1 EQE gain target over baseline @ 100A/cm^2 | T_j=85°C	NIST calibrated efficacy measurement at T_j=85°C	M12	Completed M13
3	Verify / improve understanding of defects in low droop structures	3.1	Compare defects within moderate and aggressive LED designs for droop improvement and determine if categorically new defects emerge	DLOS spectroscopic data and deep-level energy assignment	M15	Completed M15
		3.2	Demonstrate controllable defect mitigation through optimized growth/design conditions for low droop structures	DLOS-LCV trap density calculation	M18	Completed with change of scope M18[b)]
4	Realization of improved high current efficiency in production ready designs	4.1	Verify that trends in defect density caused by changes in growth process are consistent between simple and complex epi designs	DLOS, STEM/3D-APT image and analytical technique analysis	M20	Completed with change of scope M20[b)]
		4.2	Year 2 EQE gain target over baseline @ 100A/cm^2 | T_j=85°C	NIST calibrated efficacy measurement at T_j=85°C	M24	Completed M24
5	Finalize LED structure and MOCVD recipe	5.1	Process freeze and beginning of production qualification	Lumileds internal qualification process milestone	M24	Completed M24

a) The assumption that particular defect(s) would emerge in different active region designs was proven incorrect so the milestones based on this idea became partially inapplicable.

b) Quantitative interpretation of DLOS-LCV trap density calculations for Lumileds samples was more difficult than had been expected based on previous experience with LEDs grown at Sandia. For comparisons across active region designs trap concentrations could not be quantified with sufficient accuracy to entirely fulfill the original scope of these milestones.

3. Project activities

3.1. Characterization of initial sample set and first iterations of epitaxy improvement

Sample growth and selection

A first set of samples were grown that were expected to exhibit varying defect densities. To accomplish this, the active region designs were changed relative to the baseline design. Figure 1 shows the low/high current EQE ratio for the first sample set. This EQE ratio is to some extent indicative of material quality particularly when comparing designs with similar carrier transport characteristics since IQE is most sensitive to SRH recombination at low drive currents.

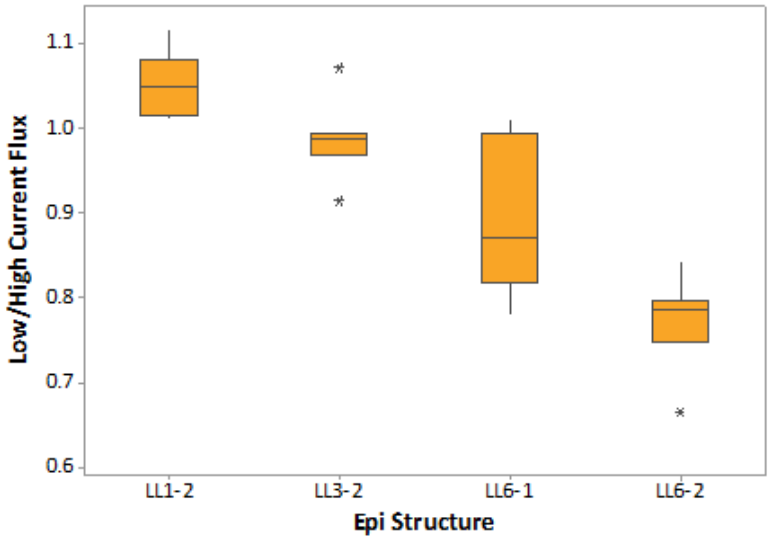

Figure 1. Low/high current EQE ratio for the first sample set.

DLOS characterization of initial sample set

A first task that had to be completed before collecting any data was to make devices with geometries compatible with requirements of the DLOS measurement system at Sandia. The standard 1mm^2 devices used by Lumileds for routine EQE characterization proved unsuitable due to their high capacitance and the need to focus the optical beam over a small area to obtain sufficient irradiance for the DLOS measurement. An alternative wafer fab process had to be implemented to produce smaller-area devices suitable for DLOS. The alternative process successfully produced devices giving useful DLOS data, but the need for non-standard wafer processing increased the time of a typical DLOS experiment cycle and meant that new wafers had to be processed specifically for DLOS.

The first step to using DLOS to understand defect incorporation in droop-mitigating active region designs was to examine three samples from the sample set introduced in the previous section. Samples LL1-2 and LL6-2 had high and low ratios of the low/high current EQE, respectively. Figure 2 shows the DLOS spectra for these two samples. DLOS measures the optical cross-section (σ^o) of sub-band gap light by deep level defects. The line-shape of the absorption was fit via the least-squares method to a theoretical model [R. Pässler, Journal of Applied Physics **96**, 715 (2004)] to determine the energy levels of the defects in the band gap. Note that the magnitudes of the DLOS spectra do not indicate relative defect densities. The similar spectra indicate that the same types of defects are found in both LEDs. Fitting the data between 1.50 – 2.3 eV determines a deep

level energy at 2.0 eV below the conduction band edge (E_c), while fitting the data between 2.70 – 3.10 eV reveals another defect state with deep level energy at 2.7 eV below Ec. A third defect state was observed at 3.15 eV below E_c from an abrupt step in the DLOS data at 3.15 eV light energy (best seen in LL1-2). Figure 3 shows the lighted capacitance-voltage (LCV) data for the LEDs, which is proportional to the defect density [A. Armstrong, M.H. Crawford, and D.D. Koleske, Journal of Elec Materi **40**, 369 (2011)]. LCV measures the increase in reverse bias (ΔV) required to increase the depletion region to a given depth when light is used to depopulate defect states [A. Armstrong, M.H. Crawford, and D.D. Koleske, Journal of Elec Materi **40**, 369 (2011)]. Light energies of 2.60, 3.05, and 3.30 eV were used to depopulate the Ec – 2.0, Ec – 2.7, and Ec – 3.15 eV levels, respectively. The larger ΔV for LL6-2 compared to LL1-2 indicates a larger defect density, even when accounting for the different active region widths, which demonstrates that a decreasing low/high current EQE ratio (Fig. 1) is associated with increasing defect density. These findings satisfied the objectives of Milestone 1.1.1.

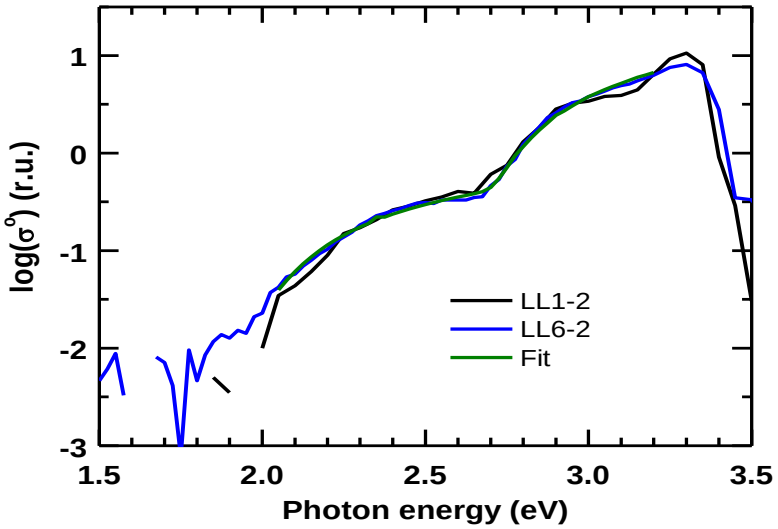

Figure 2. DLOS comparison of LED designs LL1-2 and LL6-2. The green line is a fit to a theoretical model.

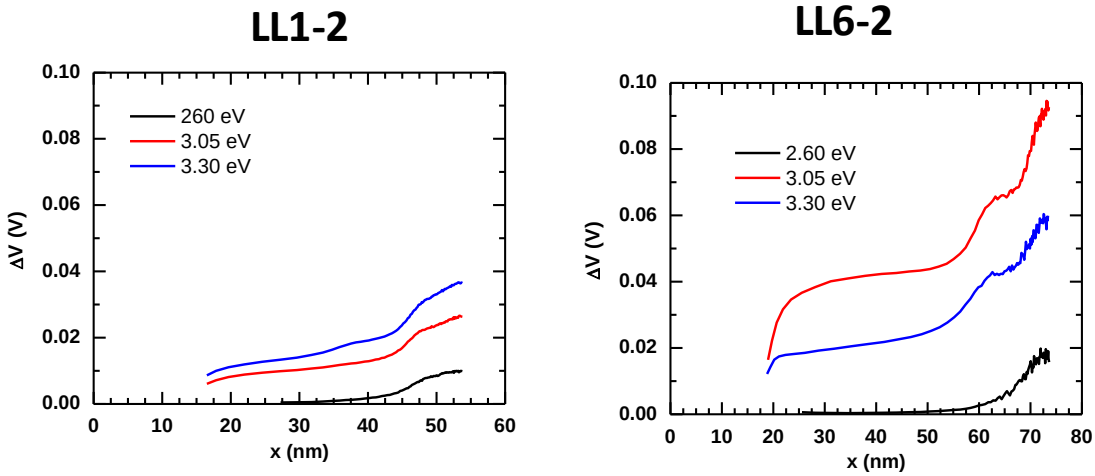

Figure 3. LCV comparison of LED designs LL1-2 and LL6-2.

The DLOS data in Fig. 2 show three deep level defects in the active region. The E_c – 3.15 eV level can be immediately ascribed to the QB because its energy exceeds the band gap of the QW. However, the E_c – 2.0 and E_c – 2.7 eV levels could potentially be related to either the QW or the QB. To distinguish between QW and QB defects, a series of LEDs were grown with nominally the same QB but different indium content in the QW. LL8 was grown with the usual QW indium content to produce 2.75 eV emission, while LL8B had higher QW indium content to emit at 2.63 eV and LL8A had less QW indium content to emit at 2.83 eV. Figure 4 shows the DLOS of the three LEDs. The DLOS spectra between 2.50 – 2.80 eV show a monotonic blue shift with increasing indium content in the QWs, so the E_c – 2.7 eV defect of LL8 was unambiguously assigned to the QWs. The DLOS spectra between 1.50 – 2.60 eV do not show obvious differences with changes to the indium content in the QWs, but the lack of clear differences in this energy range has more than one possible interpretation. While the optical ionization energy of a comparatively shallow level such as the E_c – 2.7 eV defect (close to the valence band maximum) increases in nearly direct proportion to the increase in bandgap energy, a weaker dependence on bandgap energy should be expected for the E_c – 2.0 eV defect. The position of a mid-gap level such as the E_c – 2.0 eV defect is typically fixed relative to the vacuum level and the optical ionization energy increases only with the fraction of the bandgap increase that occurs in the conduction band. Therefore, an argument could be made that both the E_c – 2.0 eV and E_c – 2.7 eV defects exist in the QWs, but the dependence of the ionization energy on the InGaN bandgap was hard to resolve for the E_c – 2.0 eV defect given its much broader spectral width and the smaller absolute shifts in energy expected for this deeper level. Unfortunately no unambiguous assignment of the E_c – 2.0 eV defect to wells or barriers was possible.

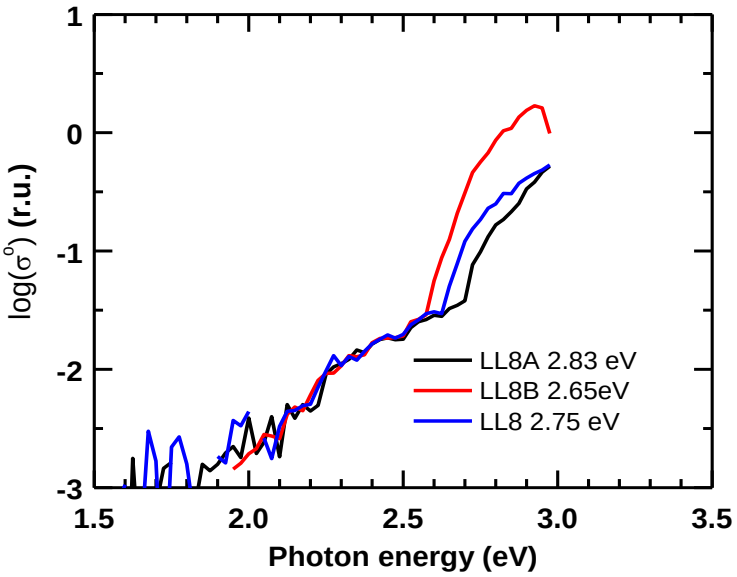

Figure 4. DLOS comparison of three otherwise similar LEDs with different indium concentrations in the QWs.

The assignment of particular electronic defect levels to locations in wells or barriers was an important first step toward understanding the tendencies of these defects to form in different growth conditions as described in Milestone 1.2.2. Identifying the atomistic nature of electronic defect levels is in general a rather speculative activity and is particularly difficult if the levels of interest are present in low concentrations, as expected for commercial-grade LED wafers. Literature studies of material grown in academia suggest that the E_c-3.15eV level might be related

to carbon impurities or nitrogen vacancies while DLOS defects with transition energies close to those of the E_c-2.7eV and E_c-2.0eV levels were suggested to be related to Group III vacancy complexes with carbon or oxygen, respectively [M. Lozac'h et al. Jpn. J. Appl. Phys. 51, 121001 (2012)]. Further study of these defects was beyond the scope of this project and would have diverted resources from pursuing the EQE improvement goals.

Atomic structure characterization of initial sample set

Electron microscopy in conjunction with other characterization techniques allows direct correlation between QW microstructure and device characteristics. For high resolution cross-sectional scanning transmission electron microscopy (STEM) imaging, thin (< 100 nm) lamellae of LED samples were prepared using a focused gallium ion beam in a Helios Nanolab system. The lamellae were thinned with successive reductions in ion beam accelerating voltages (30 kV, 16 kV, 5 kV, 2 kV) to minimize beam damage and ion implantation. The final step at 2 kV removes surface amorphization. STEM was performed using either an FEI Titan or Hitachi 2700C, operating at 80 kV or 120 kV respectively. Importantly, the accelerating voltage was maintained below knock-on damage threshold for InGaN alloys to prevent beam-induced structural changes. Four samples with differences in the active region design and/or growth conditions were included in the initial sample set.

Threading dislocations were the only extended defects observed in low-magnification images (not shown). These dislocations originate very far below the active region and their presence is an inevitable consequence of the heteroepitaxial growth of GaN on sapphire. Fig. 5 shows high magnification STEM images of the light-emitting active regions of three LEDs included in a comparative study. Since mass-thickness is the dominant contrast mechanism, InGaN QWs appear brighter compared to GaN barriers in these dark field images. The most obvious difference between the samples was the presence of well-width fluctuations in some samples but not in others. The relationships between well-width fluctuations, growth conditions, and EQE were not clear from this preliminary study. However, as will be discussed in Section 3.2 below, it was later shown that the MOCVD growth conditions have a strong impact on well-width fluctuations for a given active region design. The results summarized in Fig. 5 satisfied the objectives of Milestones 1.1.2 and 1.2.1.

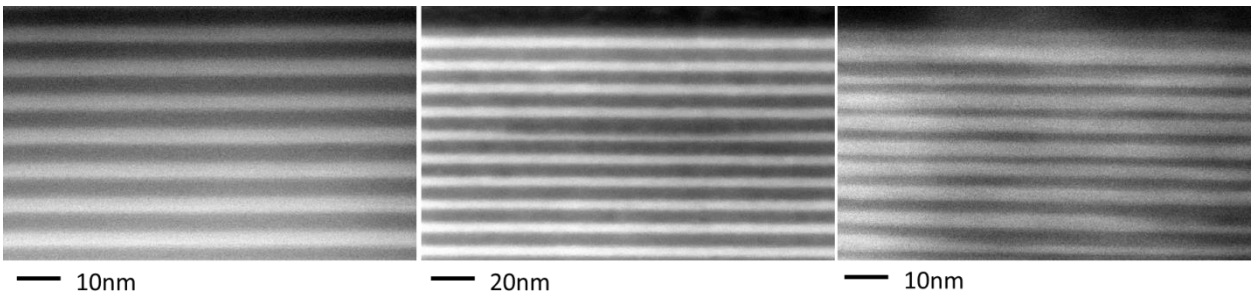

Figure 5. Dark-field STEM cross-section micrographs for samples LL6-1 (left), LL9 (center) and LL6-2 (right). Note that LL9 was imaged at lower magnification than LL6-1 and LL6-2.

Epitaxial growth improvement

Significant improvements in performance were achieved using new MOCVD growth processes. A simplified device structure was used for this study. The chosen structure is not optimized for

droop reduction but its reduced complexity allows for unambiguous correlation of material quality changes directly to EQE. Improvements were observed at various stages of characterization from photoluminescence (Fig. 6) up through and including EQE measurements of packaged high power LEDs (Fig. 7). The low current performance (Fig. 7a) improves by >30% over the baseline at 2A/cm^2 with this new process which comfortably exceeds the Milestone 1.3.1 target. At high current (Fig. 7b) the gains diminish as would be expected assuming the only difference associated with the improved process was a reduction in the SRH recombination rate. We also found that QWs grown with the new process appear to be more homogenous as inferred by the narrower full-width at half maximum (FWHM) of the LED emission spectrum compared to that of the baseline process (Fig. 7c).

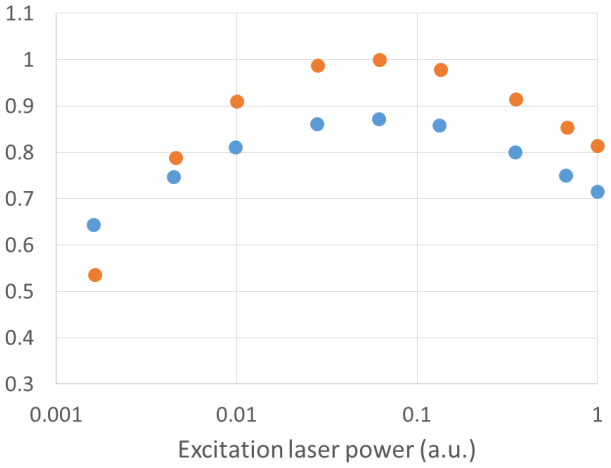

Figure 6. Normalized photoluminescence efficiency for two samples with identical structure but different MOCVD process conditions. The improved process shown by orange circles shows significant gains in material quality (improved efficiency at low and intermediate excitation laser powers) as compared to the baseline process shown by blue circles.

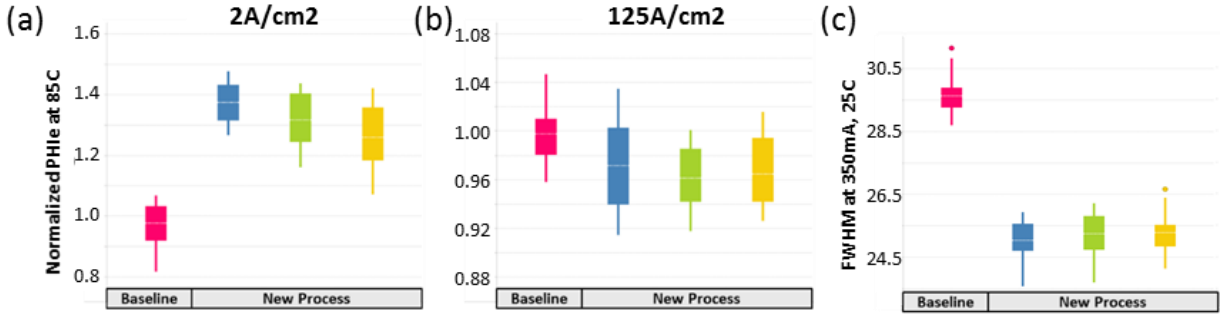

Figure 7. Low current (a) and high current (b) radiant flux of samples grown using different MOCVD processes. c) FWHM of the emission peak of the same samples.

Evaluation of improved droop concepts

Device modeling was used to design low droop structures which were later grown and evaluated experimentally. The first design seeks to improve hole transport and is shown in Figure 8a. The

hole density in each QW is shifted toward the n-side of the device in the orange curve (new design), reducing the carrier density in the p-side QWs. This results in a calculated IQE improvement at 100A/cm^2. The other concept studied in modelling improves the radiative recombination rate in the p-side QWs where most of the recombination occurs. An increased radiative rate reduces the carrier density in the QWs, further improving their efficiency by reducing Auger recombination. The new design improves the electron/hole overlap in the last two QWs (Fig. 8b), resulting in an IQE improvement at 100A/cm^2.

Both concepts were evaluated experimentally, as was the combination of the two designs (Fig. 9). The improved hole spreading and improved radiative rate design changes both resulted in modest gains of ~1.5% and ~2% over the baseline, coming slightly lower than gains predicted by the model. The exact quantitative agreement is less important than the fact that the experimental trends match the model results. The structure that combines both of these specific droop improvement changes suggested by modelling was also grown, and resulted in ~3% EQE gain at 125A/cm^2. The results summarized in the previous two paragraphs meet the requirements for Milestone 1.4.1.

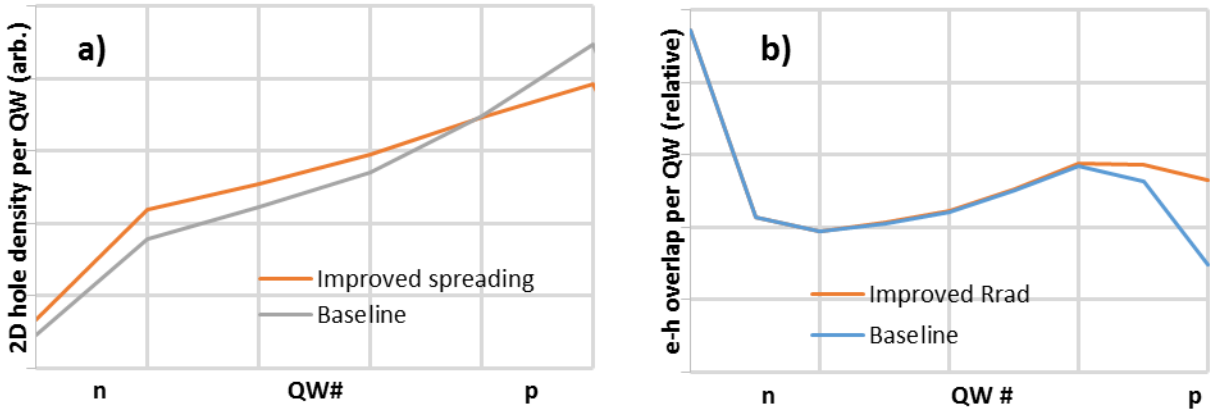

Figure 8. a) Calculated 2D hole density per QW and b) electron hole overlap per QW of two structures that improve droop

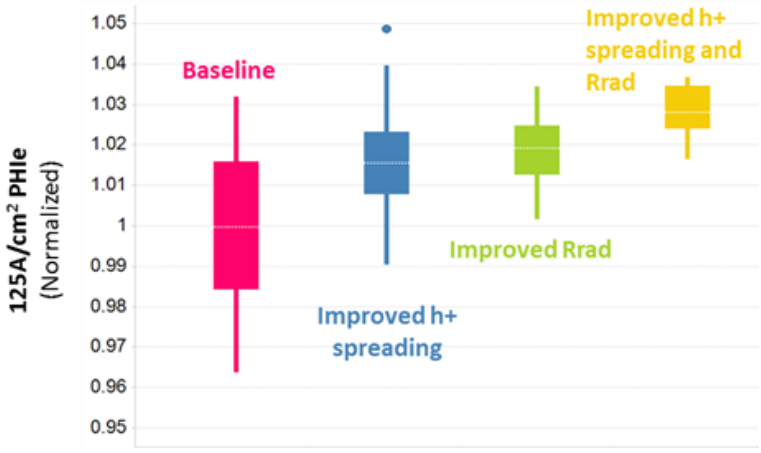

Figure 9. Experimental high current flux of several LEDs that use improved droop concepts developed using computational modelling.

3.2. Correlating emergent defects to growth conditions

Growth Condition A

In this section we will discuss as an example the effects of one particular change in growth conditions (Growth Condition A) on structural defects and electronic defects in the active region and their impact on device performance.

STEM images from two samples that highlight the effect of Growth Condition A are shown in Fig. 10. The image on the right is from the sample LL9 previously presented in Fig. 4. The image on the left of Fig. 10 is from the growth run LL7 that reproduced the same active region design as LL9 using different growth conditions. For sample LL9 obvious fluctuations in the well width are observed and sections of the wells are completely missing in some parts of the structure. In contrast, LL7 shows very consistent well widths across each period with no evidence of missing wells in any parts of the structure. From these observations, it was concluded that well width fluctuations are not an inevitable consequence of specific active region designs, but rather can be mitigated by changing growth conditions.

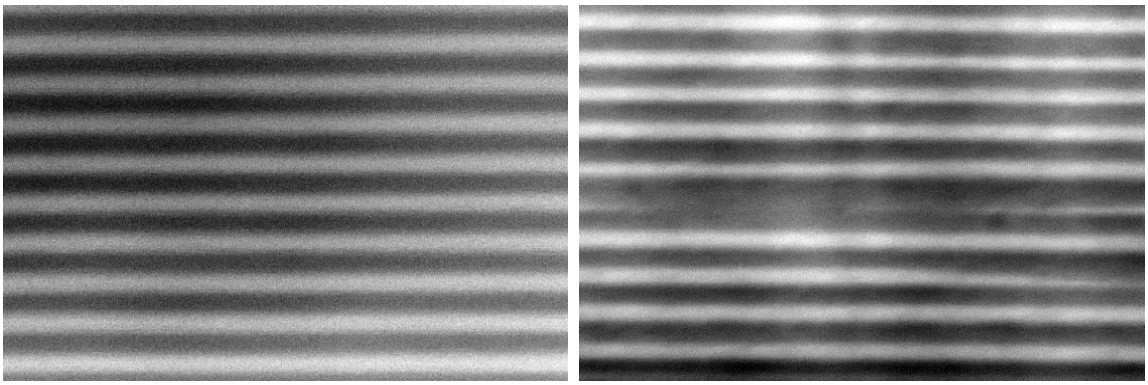

Figure 10. Dark-field STEM cross-section micrographs for samples LL7 and LL9 which show the same active region design produced with different growth conditions. Note that the magnification is not exactly the same in the two images.

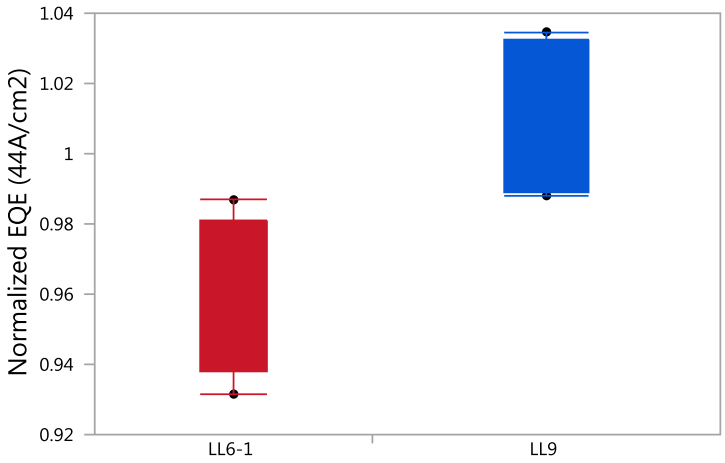

Figure 11. Relative EQE at the current density of 44A/cm^2 for the sample LL6-1 (no fluctuations) and the sample LL9 (moderate fluctuations).

Surprisingly, EQE measurements of the LEDs (Fig. 11) indicated slightly better performance for the sample *with* well-width fluctuations. This result implies that the appearance of fluctuations is not the primary reason for the increased density of SRH recombination centers in droop-mitigating active region designs. The DLOS results for samples LL7 and LL9 are shown in Fig. 12. There is a clear difference in the concentrations of the 2.7eV level between the samples but no significant difference in the concentrations of the 2.0eV and 3.15eV levels. It appears that Growth Condition A has a clear effect on both the extent of well-width fluctuations and the concentration of the 2.7eV level, but neither of the above types of defects has a strong impact on device performance.

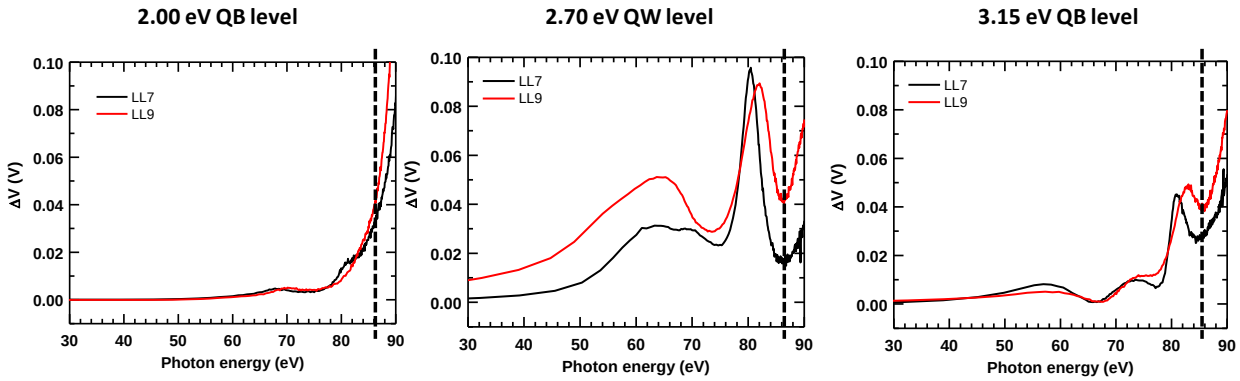

Figure 12. LCV comparison of LEDs LL7 and LL9 with the same active region design but different growth conditions (Growth Condition A).

Growth Condition B

In the present section we will discuss changes to a growth variable (Growth Condition B) which had a large impact on EQE. Samples LL10 and LL11 are similar in structure (same number of layers and layer thickness in the active region), but differ in growth conditions (Growth Condition B). The growth variables changed in B were not the same as those discussed in A above. The EQE values of the samples as a function of current density normalized to the performance of sample LL11 at each current density are shown in Fig. 13. Sample LL10 shows extremely poor low-current efficiency (5 times worse than LL11) and still quite poor high-current efficiency (40% worse than LL11). The data in Fig. 13 represent the largest difference in performance between any of the samples studied in this project.

High-resolution TEM cross-section micrographs for the samples LL10 and LL11 are shown in Fig. 14. Despite the large differences in EQE, no obvious differences were observed in the high resolution TEM images or STEM images of the same samples taken at lower magnification (not shown). DLOS and LCV were performed on the two LED samples to assess how the change in Growth Condition B impacted deep level defect incorporation. The DLOS spectra of the LEDs are shown in Fig. 15. The line-shapes of these LEDs are similar to those of previously studied samples discussed above, which suggests that the same types of defects observed earlier still incorporate in the active regions of LL10 and LL11. However, the DLOS spectra between 1.50 – 2.60 eV are poorly resolved for LL11 suggesting a low defect density near the detection limit in this sample. LCV measurements shown in Fig. 16 were performed to compare better the defect densities of LL10 and LL11.

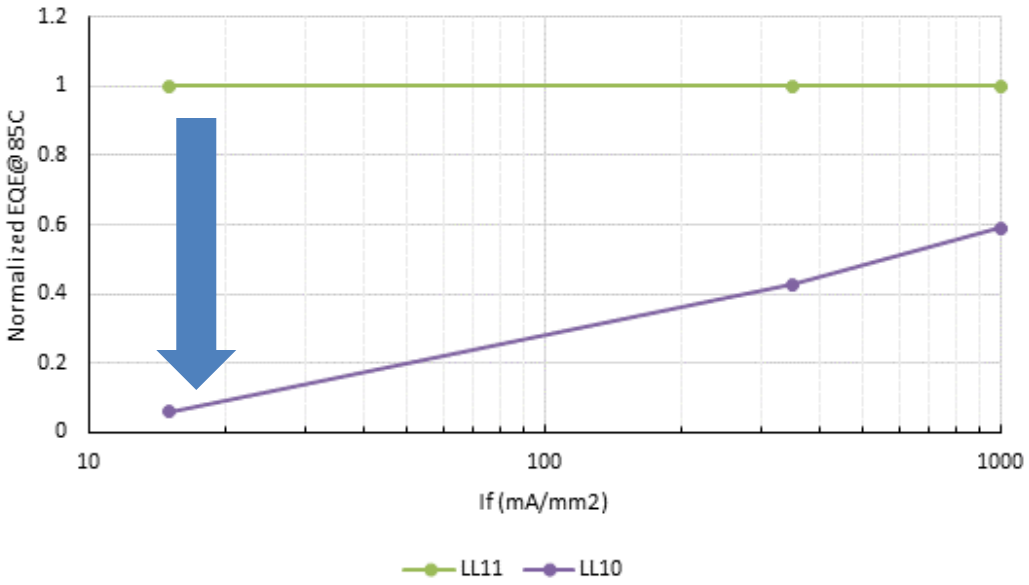

Figure 13. EQE as a function of current density for samples LL10 and LL11 normalized to the LL11 value at each current density.

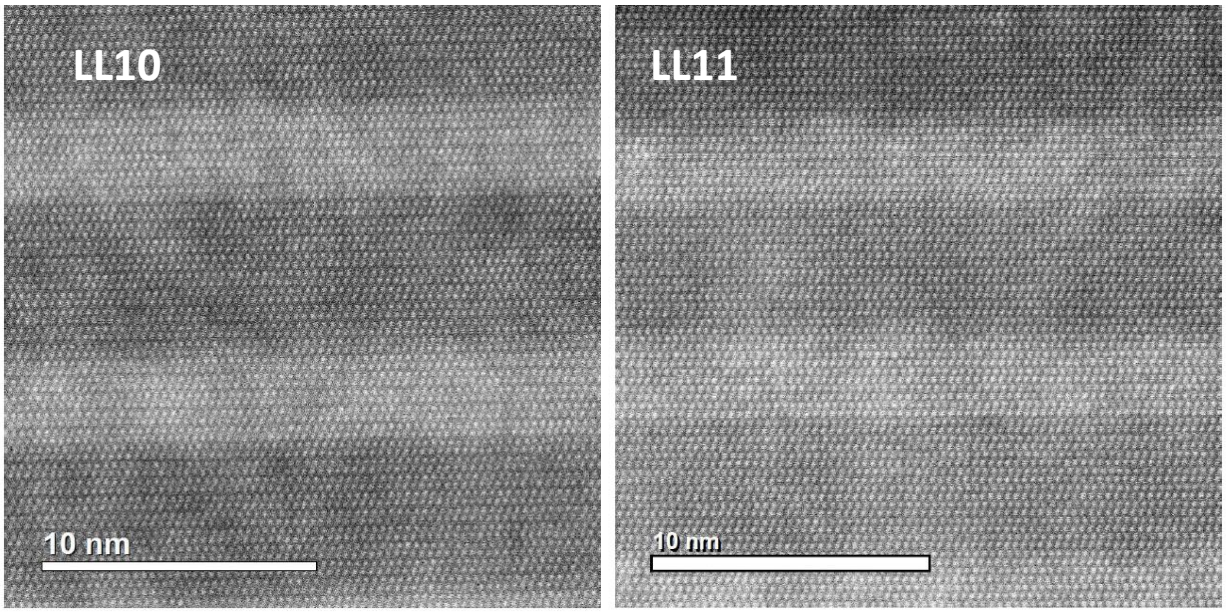

Figure 14. High-resolution TEM cross-section micrographs of samples LL10 and LL11 with change in Growth Condition B. Note the scale bars are not exactly the same in the two images.

The vertical dashed lines in Fig. 16 correspond to the position where the ΔV signal originates from active region defects versus defects located in layers beneath the active region. The extent of the nominal active region was only 48 nm, however, ΔV data at a depth of 50 nm were attributed to the active region. This demarcation is justified by one-dimensional Schrodinger-Poisson calculations that were completed to interpret the LCV data. Fig. 17 shows a one-dimensional Schrodinger-Poisson simulation of LL10 for an arbitrary defect density of 5×10^{16} cm^{-3}. The analytical value of ΔV for this defect concentration is 0.0375 V, however, the simulation shows an overshoot in ΔV before reaching the correct value. Further, the calculated ΔV data reach the

correct value at a depth of 52 nm, which is deeper than the defined active region. Thus, these spikes were ignored when comparing defect density, and the calculated result justified using an experimental ΔV demarcation that is at a depth beyond the edge of the nominal active region. The inflection points at the dashed lines in Fig. 16 occur because the ΔV associated with active region defects has plateaued, while defects from layers below the active region begin to contribute to ΔV.

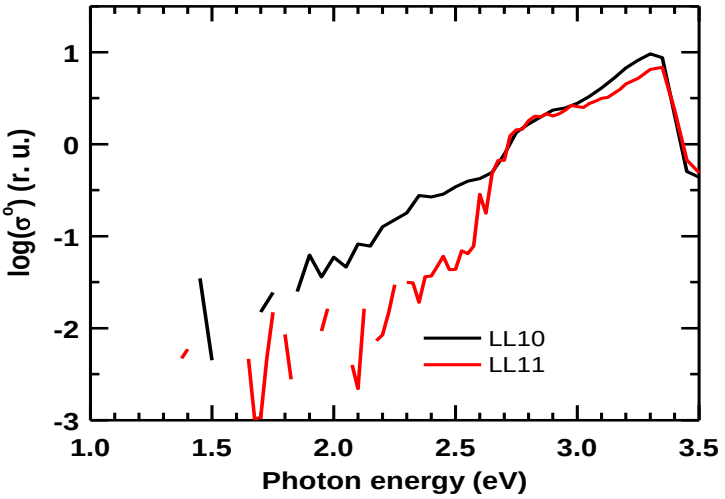

Figure 15. DLOS comparison of LEDs with change in Growth Condition B

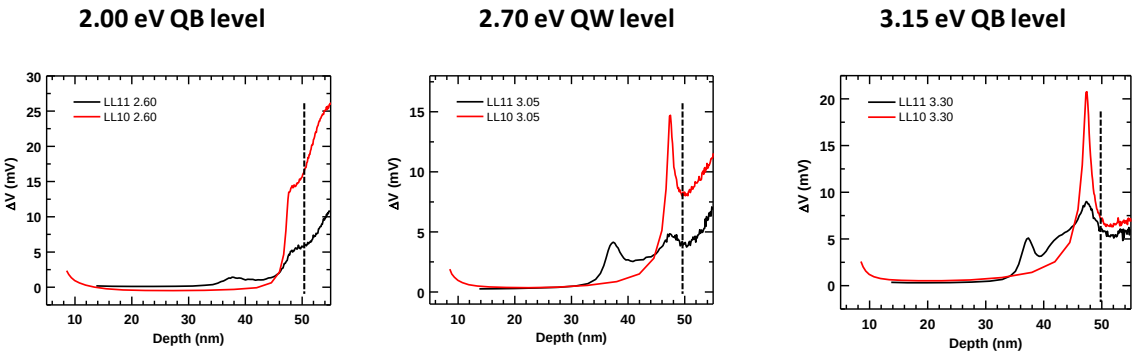

Figure 16. LCV comparison of defects in LEDs LL11 and LL10 with change in Growth Condition B.

The active region width was the same for both LEDs, so the ratio of ΔV is the same as the ratio of defect densities in these LEDs. The 3x larger ΔV for the E_c – 2.0 eV level and 1.5x larger ΔV for the E_c – 2.7 eV level observed for LL10 demonstrate a higher defect density in this LED. From the combined dataset of all samples studied it can be tentatively concluded that the E_c – 2.0 eV level is an important defect related to SRH recombination while the E_c – 2.7 eV and E_c – 3.15 eV levels are of less importance. This conclusion is supported by the observation that large differences were sometimes observed in the concentrations of the E_c – 2.7 eV and/or E_c – 3.15 eV levels between samples that showed closely comparable EQE (such as LL7 and LL9 in Fig. 12). On the other hand a large difference in the concentration of the E_c – 2.0 eV level was observed only for sample LL10 which had extremely poor low current EQE compared to all other samples in the study.

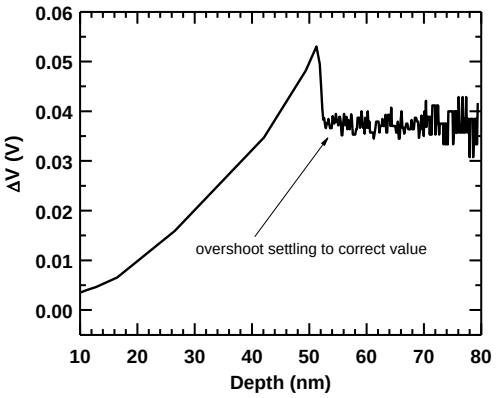

Figure 17. One-dimensional Schrodinger-Poisson calculation of ΔV data showing an artifact of overshoot near the edge of the active region.

In this section and the previous one we have reviewed a few illustrative examples of how changes in growth conditions were related to features detected using advanced characterization techniques and correlated to final lamp EQE measurements in line with the objectives given in Milestones 2.1.1 through 2.2.2. In some cases defects were observed that did not appear to be very important for device performance (Growth Condition A). It was an unexpected result that large differences in EQE measurements did not correlate well with observations of structural differences (or lack thereof) in high-resolution TEM and STEM images. This learning was valuable for future practical development toward the project EQE goals but did require some adjustments to the plan of work that had been originally outlined in the project proposal. Specifically, in subsequent work less emphasis was placed on purely structural characterization techniques and more use was made of characterization techniques that directly probe the optoelectronic properties of the material, such as cathodoluminescence.

Cathodoluminescence investigations

Cathodoluminescence in a scanning electron microscope (SEM-CL) is an interesting technique that may complement the STEM and DLOS techniques introduced in previous sections of this report. SEM-CL can be used to quickly characterize comparatively large areas of the sample and might be used to identify specific areas of interest for advanced nanoscale structural characterization with TEM-based methods. SEM-CL was measured in a JEOL JXA-8200 Superprobe operated at accelerating voltages of 10-25 kV. The beam current was varied between 0.5-10 nA to study the effect of charge injection rate on CL rise dynamics. The cathodoluminescence was collected by a parabolic mirror situated just above the sample. Each LED sample was exposed to a stationary electron beam over the course of 200 s, and SEM-CL spectra were acquired once per second (with 100 ms integration time) under continuous spot mode illumination (100 nm probe diameter).

An interesting and unexpected result was observed in the SEM-CL studies of LED samples. In most cases the luminescence signal from the QWs showed a time delayed response, while there was no delay in the response of the luminescence peaks from other layers in the structure that are not part of the active region. This behavior is expressed in Fig. 18 which shows contour plots of the luminescence at particular wavelengths as a function of electron beam exposure time for four different samples. The QW luminescence peak is near 450nm while the peak near 400nm corresponds to a dilute InGaN layer outside of the active region.

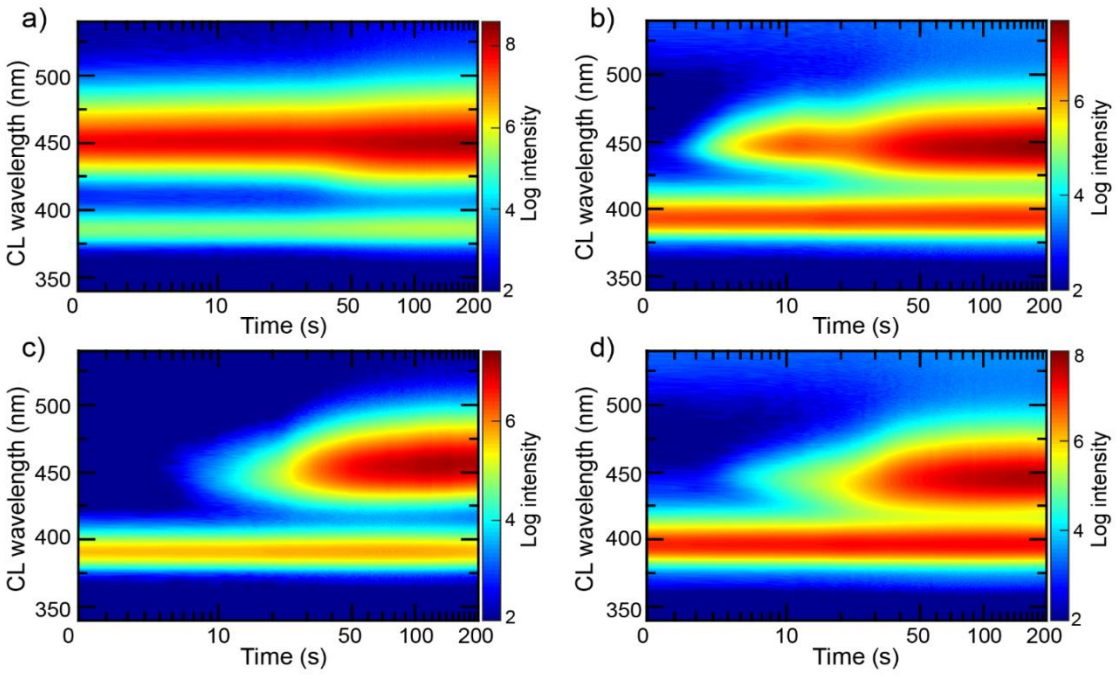

Figure 18. Contour plots of cathodoluminescence intensity at a particular wavelength as a function of electron beam exposure time for four different LED samples.

For the sample in the upper left plot of Fig. 18 intense luminescence is observed at 450nm from the very beginning of the measurement, but in the other three samples there is no 450nm luminescence detected at time zero and it takes many tens of seconds before a steady state luminescence intensity is reached at that wavelength. A proposed physical model that qualitatively explains the observed time-dependent SEM-CL data is illustrated in Fig. 19.

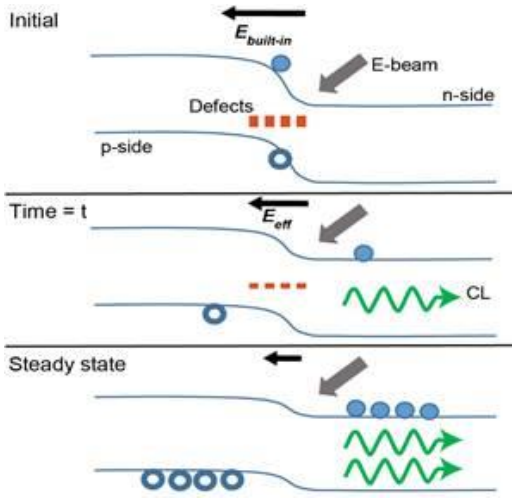

Figure 19. Diagrams related to physical model proposed to explain time-dependent QW luminescence signals in SEM-CL.

The studied LEDs can be approximately described as p-i-n junctions since the doping in the MQW active region is much lower than the doping in adjacent GaN layers. When the electron beam is initially incident on the sample, electron-hole pairs generated inside the QW active region are swept apart by the built-in field of the junction, preventing radiative recombination. These separated carriers produce a time-dependent counter-voltage that reduces the built-in field. As carriers are continuously generated under the electron beam the above effect intensifies until the junction reaches a steady-state open-circuit voltage. Thus, carriers generated at later times are more likely to undergo radiative recombination within the QW region due to the decreased junction field. Consequently, the QW emission intensity increases over time until steady-state is reached.

Some differences between the four samples shown in Fig. 18 can be understood in the context of the model illustrated in Fig. 19 and details of the different active region designs of the samples. With no external bias the electric field in the intrinsic region of the p-i-n diode is proportional to the built-in voltage divided by the thickness of the intrinsic layer. The built-in voltage is fixed by the doping concentrations on the n- and p-sides which do not differ in any of the samples studied, so the electric field in the QW region is inversely proportional to the total thickness of the (approximately intrinsic) active region. The sample at the upper left of Fig. 18 is the one with the largest total thickness of the active region and it can be surmised that the built-in electric field was not strong enough for the carriers to efficiently escape the active region in this sample, resulting in high 450nm intensity beginning at time zero. For samples with similar total active region thickness there appears also to be some dependence of the luminescence time delay on details of the calculated active region band structure, as would be expected for the carrier escape process central to the proposed model.

In summary, analyzing the time delay for samples with different active region designs provided some new information that was useful for quantifying the electric field across the active region and comparing the effectiveness of different types of barriers at confining carriers. However, it should be recognized that the carrier escape phenomenon in SEM-CL is related to the reverse bias band structure which differs from the band structure in forward bias LED operation. The reader is referred to a separate publication for further details of this project activity [Zhibo Zhao, Akshay Singh et al. manuscript in preparation].

Evaluation of updated growth conditions in complex LED device designs

Some of the learning discussed in the previous sections was leveraged to improve the material quality of droop mitigating active region designs. Figure 20 shows the low current (a) and high current (b) radiant flux of a baseline structure, a structure expected to improve droop that showed a material quality penalty (blue) and an improved droop structure with a growth condition change that eliminated the material quality penalty (green). Given the timeline for realizing the project EQE improvement goals, the result shown in Fig. 20 was to some extent achieved through empirical work, but the reasons underlying the improvement could be better understood by applying the STEM and DLOS techniques. The improvement shown in Fig. 20 contributed partially to fulfilling the Milestone 2.4.1 but other design changes building on the improvements demonstrated in Fig. 9 above were also required to achieve the full Year 1 EQE gain target milestone.

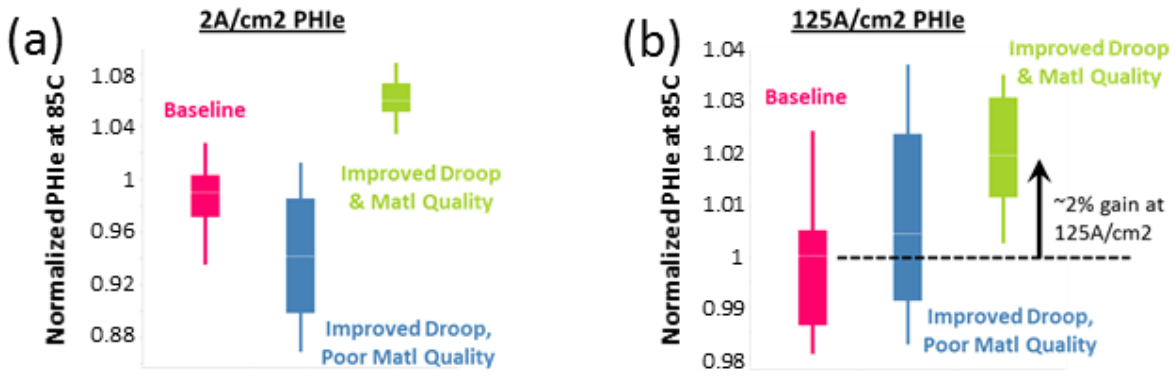

Figure 20. Low current (a) and high current (b) normalized radiant flux of various LED epi structures.

3.3. Verify and improve understanding of defects in low droop structures

Continuing DLOS studies

DLOS spectra of various LED samples with differences in both active region designs and growth conditions were measured to determine if new types of defect emerged . Fig. 21 shows the DLOS spectra of this group, where all the LEDs exhibited essentially the same deep level optical cross-section line-shape. Thus, no new types of defects were observed even in the most extreme designs investigated. This conclusion completed the work required for Milestone 3.1. The hypothesis suggested in the original proposal that new types of defects might emerge in droop-mitigating active region designs was proven incorrect.

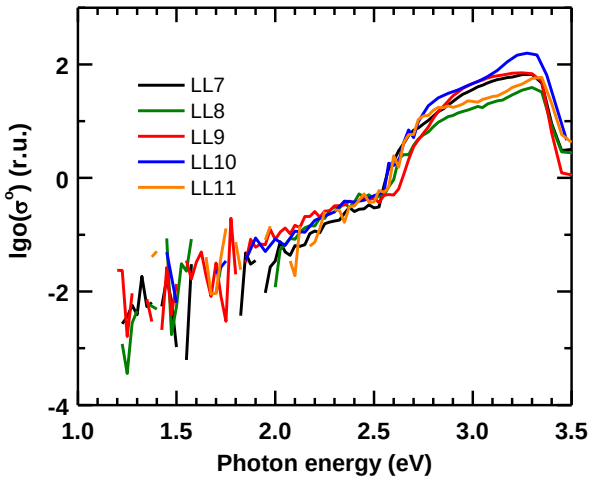

Fig. 21. DLOS comparison of LEDs with various differences in active region designs and/or growth conditions. No significant change in the DLOS was evident.

3.4. Verify that trends in defect density caused by changes in growth process are consistent between simple and complex epi designs

The scope of work related to Milestone 4.1 needed to be changed to the extent that the actual outcome of experiments differed from assumptions that had been made in the project proposal. DLOS and LCV were used successfully to understand relatively large EQE differences between

samples with simpler designs, but we were not able to develop confidence in these techniques for accurately quantifying smaller differences in defect densities between more complex designs. STEM analysis earlier in the project did show some trends between growth conditions and structural defects in the active region (well-width fluctuations). However, it appeared unlikely that the overall project goals would be advanced by trying to verify these trends in more complex epi designs since the extent of well-width fluctuations observed in STEM did not correlate with the EQE in simpler designs.

For the reasons given above, resources in this stage of the project were allocated to different activities rather than attempting to verify trends in defect density with growth conditions in more complex structures.

3.5. Additional accomplishments beyond stated project milestones

It was concluded from the results described in Section 3.2 above that the EQE sensitivity to Growth Condition B should be attributed to changes in concentrations of point defects that are not detectable in STEM or high-resolution TEM images. Further epitaxy process development toward achieving the project EQE goals was based on the above conclusion, but some additional structural characterization work did continue later to see if any subtle differences might be detected between the two samples with a large EQE difference (LL10 and LL11) using more advanced techinques.

Statistical analysis of interface roughness in HR-TEM data

We applied statistical methods to measure interface quality in samples LL10 and LL11 from atomically-resolved scanning transmission electron microscopy (STEM) images. The images shown previously in Fig. 14 are representative of some of the images analyzed statistically in this later additional work. Intensity of STEM images representing individual rows of atoms were extracted by measuring the STEM intensity line profile across a given row of atoms and obtaining the local maxima values at each atomic position. These intensities are modelled as a random variable reflecting the composition and uniformity of a single row of atoms. Therefore, different rows of atoms within the same STEM image can be compared to determine their similarity/dissimilarity in a statistically significant manner.

Since dark-field STEM intensity depends strongly on mass-thickness contrast, comparing the means of STEM intensities in two different rows allows a comparison of average composition between those rows of atoms (assuming no large changes in sample thickness). Two types of statistical tests were applied to the data of interest: Welch's t-test and the Kolmogorov-Smirnov test [Eadie, Drijard, James, Roos, and Sadoulet, *Statistical Methods in Experimental Physics*, Amsterdam:North-Holland (1971)] .

We apply the methods described above to two STEM images of LL10. First, the statistical tests correctly identify that two rows of atoms in the GaN barrier are in fact constituents of the same region. Additionally, our tests can correctly distinguish rows in the middle of the GaN barriers from rows in the middle of the InGaN QWs by identifying statistically significant differences in the sample means between two such rows. In one STEM image these tests indicated that the GaN and InGaN layers at the interface between the barrier and QW are different from the GaN and InGaN layers in the interior of the barrier and QW regions, respectively. However, the GaN and InGaN layers at the top and bottom interfaces are statistically similar to each other. Hence, the analysis suggests a structural difference at the interfacial layers in comparison to the QW/barrier interiors, while in this particular region of the QW, the top and bottom interfaces do not exhibit

strong differences from each other. In another STEM image the analysis again demonstrated that GaN layers in the interior of the barrier region are distinct from the GaN layers at the interface. Further, in this particular region, the top and bottom interfaces are different from each other, in agreement with literature reporting differences in roughness between these two interfaces in other InGaN/GaN QW heterostructures. Notably, Welch's t-test does not draw a distinction between InGaN layers in the interior of the QW and those at the interface, while the K-S test does indicate that these layers are different. The discrepancy here arises from the characteristics of the tests as described above—although the means (average composition) of these layers are statistically similar, the variance (uniformity) remains different.

The same statistical methods are applied to a STEM micrograph of LL11 to investigate any differences in interface quality between LL10 and LL11. Note that the STEM images of LL10 and LL11 cannot be directly compared since they were taken at different times with slightly different imaging conditions. Without normalizing with respect to the intensity of the incident beam, these small differences in imaging conditions render a comparison of raw STEM intensities meaningless. Nonetheless, the quality of interfaces within the LL11 sample can still be quantitatively assessed. In this region, the GaN interfacial layers are similar to each other, but the InGaN interfacial layers are different from each other. Furthermore, the InGaN layer at the bottom interface is similar to the InGaN layers in the interior of the QW, while the InGaN layer at the top interface is different from the InGaN layers in the QW interior. These comparisons suggest that the bottom interface is sharper or more well-defined than the top interface.

Notably, we observe certain discrepancies in comparing the GaN layers in the interior of the barrier with interfacial GaN layers. In particular, some interior GaN barrier layers are categorized as statistically similar to interfacial GaN layers, while other interior GaN barrier layers are categorized in the opposite manner. Such discrepancies may reflect subtle differences between layers within the interior of the GaN barrier or may be an artifact of non-Gaussian noise within the image. A definitive understanding of these differences would require further analysis using complementary techniques such as electron energy loss spectroscopy (EELS).

In conclusion, there are no obvious differences in the interface quality between LL10 and LL11. On the other hand, the atomic layers at the QW/barrier interface are structurally distinct from layers in the interior of the QW and barrier regions. Finally, certain regions demonstrate differences between the top and bottom QW/barrier interfaces. These observations of the interface quality are consistent with existing literature, and additional studies would focus on complementing these STEM analyses with EELS measurements in order to produce a more comprehensive understanding of compositional variations at the QW/barrier interfaces.

Investigation of QW compositional uniformity using EELS

We used electron energy-loss spectroscopy (EELS) in the scanning transmission electron microscope (STEM) to investigate the spatial extent of indium fluctuations within the InGaN quantum wells of a lower-performing LED and a higher-performing LED. EELS provides the compositional fingerprint of a sample with near-lattice resolution by analyzing the energy distribution of electrons passing through the sample. This technique is also less sensitive to surface modification by sample preparation than STEM analysis. Therefore, EELS allows us to perform sub-nanoscale composition mapping of the QW regions to investigate indium clustering, indium fluctuations, atomic scale defects, and potential correlations with efficiency.

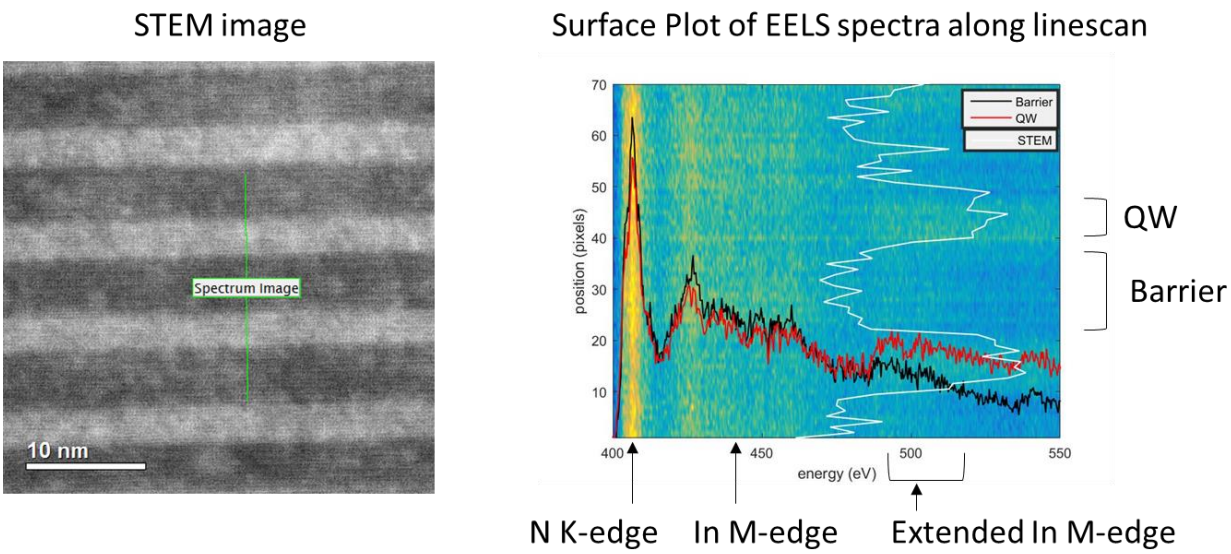

Figure 22. STEM cross-section micrograph and EELS surface plot for sample LL11.

EELS analysis of LL10 and LL11 at a beam energy of 120 keV does not reveal significant differences between compositional fluctuations of indium on the nm scale in either of these samples. In fact, the variations in In composition above the spectral noise level are minimal. To compare the In composition of LL10 and LL11, thin lamellas of each sample were prepared, and spectral EELS maps were collected on the quantum well region of each lamella. The high energy region of an EELS spectrum contains peaks corresponding to electronic transitions of inner-shell electrons to empty states above the Fermi level; therefore, relative elemental composition can be determined from the EELS data.

To extract compositional information from the EELS spectrum, the background preceding the N K-edge was fit to a power law function and subtracted, leaving the N and In edges more well-defined. Next, the spectral regions encompassing the N K-edge and In M-edge are integrated. By comparing the integrated intensity of the N and In edges at each pixel, we can determine the relative compositional fluctuations within the mapped region. The image on the right side of Fig. 22 shows spectra obtained from the QW region and barrier region of LL11, overlaying a surface plot of a linescan spanning several QWs and barriers. It is clear from the spectra that regions with a greater In composition display a broad peak around 480-540 eV. The high-intensity regions on the surface plot in the In region of the spectrum correspond to the QWs and barriers in the spatial dimension – the QW regions appear brighter whereas the barrier regions appear darker. Binning adjacent linescans helps to improve signal-to-noise as illustrated in Fig. 23.

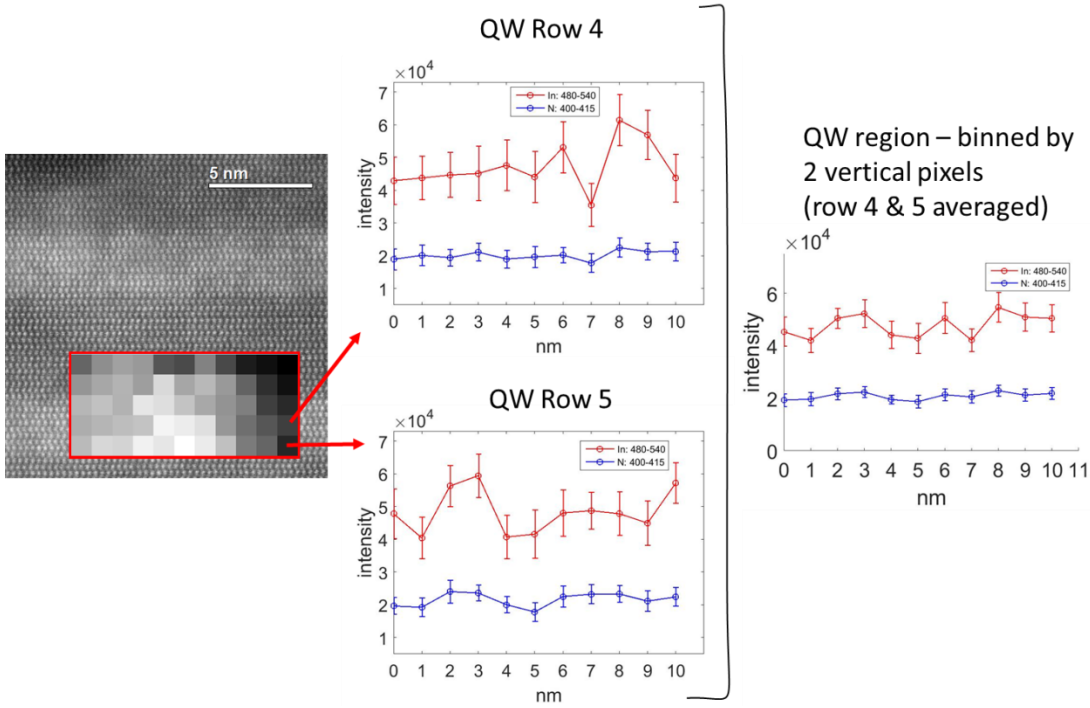

Figure 23. Illustration of how binning was used to reduce the impact of noise in EELS analysis.

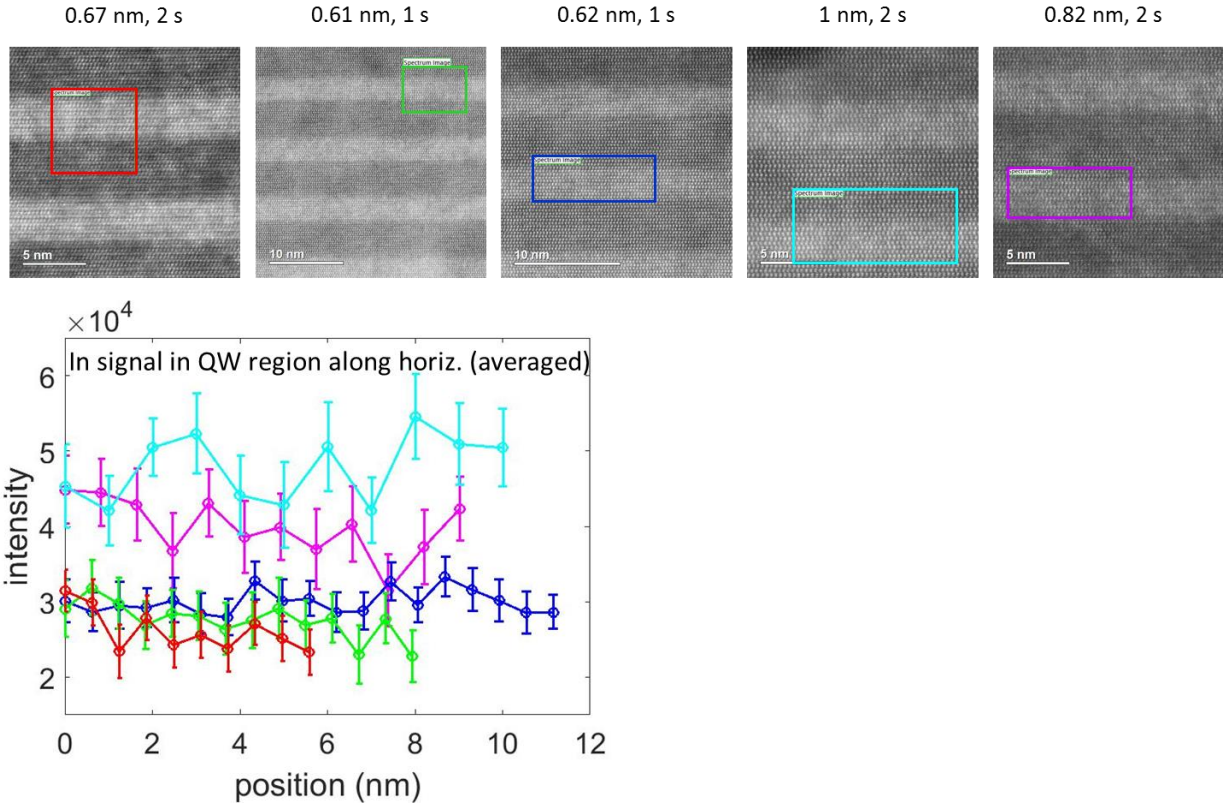

Figure 24. Line profiles of the In signal along the QW region extracted from 5 areas in sample LL11. Colors of rectangles in the STEM cross-section micrographs match colors of line profiles in the graph.

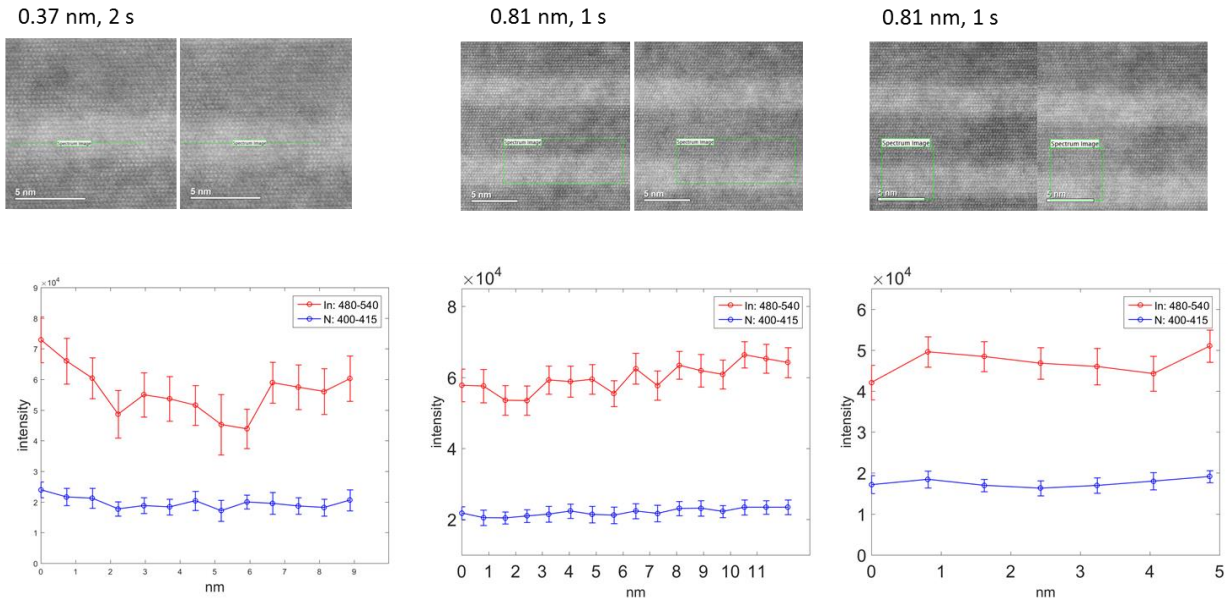

Figure 25. Line profiles of the In signal along the QW region extracted from 3 areas in sample LL11.

Fig. 24 shows line profiles of the In signal along the QW region extracted from 5 areas in LL11, with step sizes between 0.6 nm and 1 nm. Only one of these linescans shows a point-to-point variation in In signal that is greater than the error due to spectral noise. When the step size between pixels is decreased to 0.4 nm or less, the In signal demonstrates a decreasing trend along the scanning direction. STEM images before and after EELS acquisition indicate that this trend could be correlated to beam damage.

Three regions were mapped in LL10, using step sizes between 0.37-0.81 nm. Again, these linescans together only show one point-to-point variation in In signal above the noise floor (Fig. 25). Comparing the LL11 maps taken with larger step sizes and the LL10 maps, we find that not only is there no appreciable In fluctuations in these samples, but there is also no apparent difference between the two samples in terms of compositional fluctuations. Conducting the same experiment at a lower beam energy would allow us to take maps with smaller step sizes without resulting in damage, which could reveal fluctuations not seen here.

3.6. EQE performance for final MOCVD process to be qualified in manufacturing

Fig. 26 shows the EQE performance vs. current density for pump blue LEDs at various stages of this project. The green and blue curves in Fig. 26 achieved the targets in Milestones 2.1 (end of Year 1 performance) and 4.2 (end of Year 2 performance), respectively. The red curve represents performance of a process that completed manufacturing qualification and the blue curve is a further improved process. In general terms, the EQE improvements demonstrated were made possible by using the collective learning from this project to alter the active region design for improved carrier transport and electron-hole wavefunction overlap, while also re-optimizing growth conditions as necessary to minimize any material quality degradation associated with the droop mitigating designs.

We presented in the preceding sections some examples of how we used modelling and advanced

characterization methods to better understand the relationships between droop-mitigating active region designs, growth conditions, and formation of defects that are detrimental to EQE. The examples illustrated in this report are by no means exhaustive and were selected from a larger body of learning developed over the course of the project. It should be emphasized that while some of the characterization techniques applied did not detect any differences that could be correlated to EQE, the work using these techniques was nevertheless valuable and did contribute to achieving the final EQE goals. In many cases the lack of a difference detected between samples helped narrow down which problems were the important ones to work on so our development resources could be better focused.

The performance of an improved green LED process developed in parallel with this project is shown in Fig. 27. Droop is a more serious problem for green LEDs vs. blue LEDs so the opportunities for EQE gains with droop-mitigating designs are even larger in the case of green LEDs. The green LED process improvements were realized using the same general strategy from this project and leveraged much of the same learning.

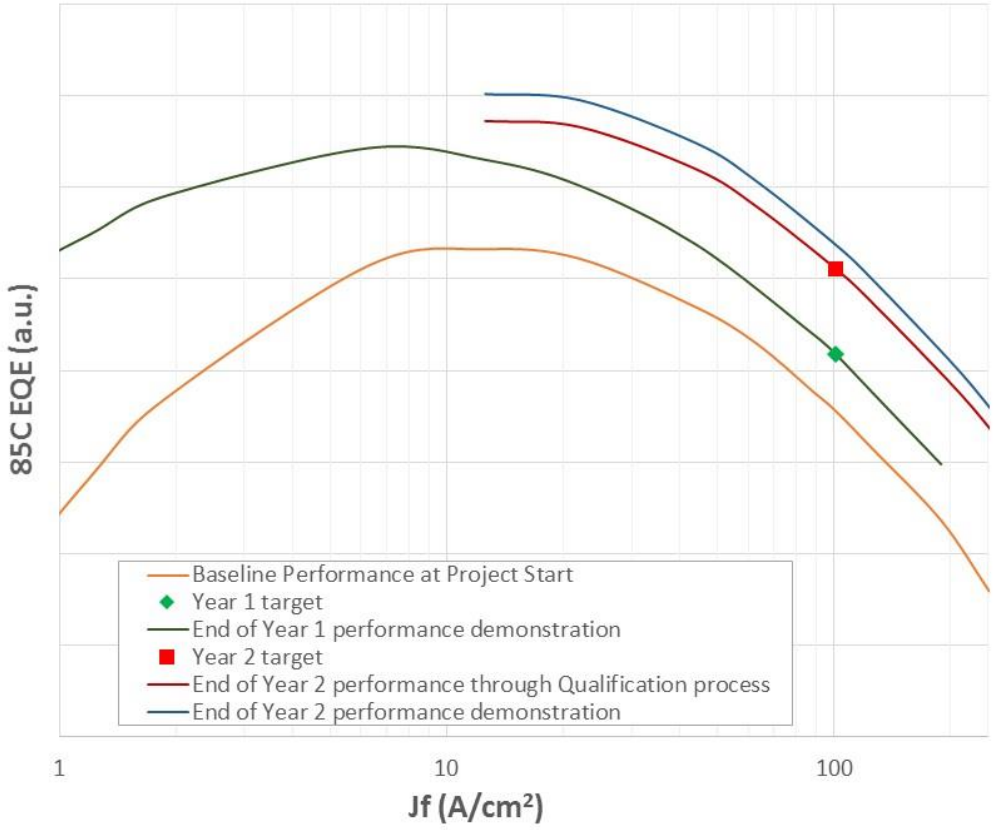

Figure 26. 85°C EQE performance vs. current density for pump blue LEDs (442.5nm peak wavelength) at various stages of the project.

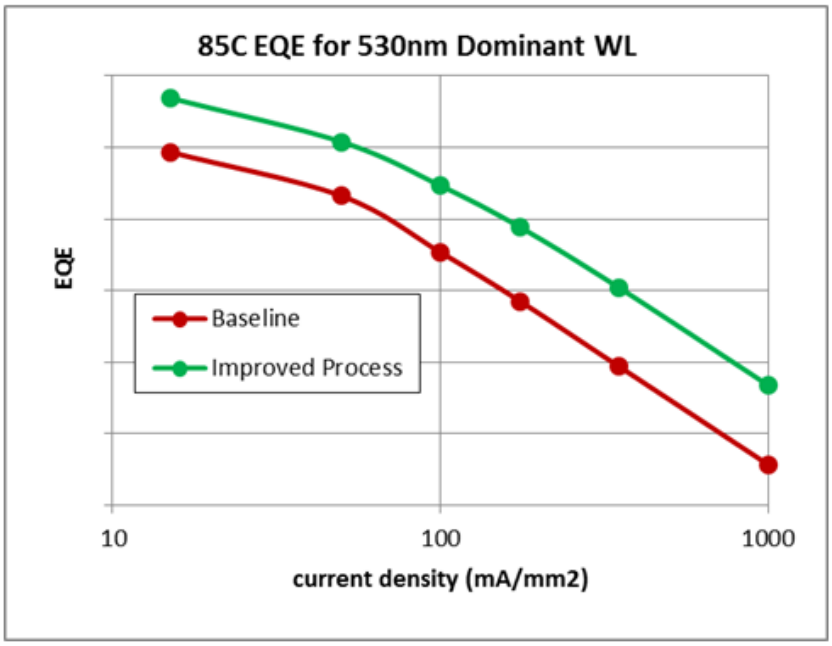

Figure 27. Relative 85°C EQE performance vs. current density for an improved green LED (530 nm dominant wavelength) process that was developed in parallel to this project and leveraged much of the same learning.

4. Products

4.1. LED products

An upgrade of our high-power royal blue epi technology for phosphor-converted illumination LEDs, based on the learnings of this project, is currently in progress. This upgrade is planned to be implemented throughout Lumileds' high-power LED illumination product portfolio.

In the color LED product space, a performance upgrade was released across Lumileds' high-power color LED portfolio in November 2017. The upgrade included substantial improvements in cyan and green performance based on the droop mitigation strategies developed in this project. Lumileds' high-power color LED portfolio includes LUXEON C, LUXEON Z Color and LUXEON Rebel Color. A press release announcing the upgrade is published at https://www.lumileds.com/news/304/50/Market-Leading-Color-Portfolio-Gets-Double-Digit-Performance-Upgrades.

4.2. Publications and presentations

1. "Mitigating Structural Defects in Droop-Minimizing InGaN/GaN Quantum Well Heterostructures," Zhibo Zhao, Jordan Chesin, Akshay Singh, Erik Nelson, Isaac Wildeson, Parijat Deb, Andrew Armstrong, Eric Stach and Silvija Gradecak, talk presented by Z. Zhao at the MRS Fall 2016 Symposium, Boston MA, Dec 2016.
2. "Improved InGaN LED System Efficacy and Cost via Droop Reduction," Andrew Armstrong, Silvija Gradecak, Eric Stach, Hee Jin Kim, Colleen Frazer, Isaac Wildeson, Erik Nelson, and Parijat Deb, poster presented by E. Nelson at the 2016 DOE SSL R&D Workshop, Raleigh NC, Feb 2016.

3. “Improved InGaN LED System Efficacy and Cost via Droop Reduction,” Andrew Armstrong, Silvija Gradecak, Zhibo Zhao, Akshay Singh, Jordan Chesin, Eric Stach, Isaac Wildeson, Rob Armitage, Tsutomu Ishikawa, Wouter Soer and Parijat Deb, poster presented by I. Wildeson at the 2017 DOE SSL R&D Workshop, Long Beach, CA, Feb 2017.
4. “Spatial and compositional dependence of deep level defects in InGaN LEDs,” Andrew Armstrong, Mary Crawford, Dan Koleske, Erik Nelson, Isaac Wildeson, Robert Armitage and Parijat Deb, Invited Talk presented by A. Armstrong at the 2017 SPIE Photonics West, San Francisco, CA, Feb 2017.
5. “Improved InGaN LED System Efficacy and Cost via Droop Reduction,” Isaac Wildeson, presented at the 2017 U.S. DOE Building Technologies Office Peer Review, Washington D.C., Mar 2017.
6. “Impacts of Carrier Transport and Deep Level Defects on Delayed Cathodoluminescence in Droop-Mitigating InGaN/GaN LEDs,” Zhibo Zhao, Akshay Singh, Rob Armitage, Isaac Wildeson, Parijat Deb, Andrew Armstrong, Kim Kisslinger, Eric Stach and Silvija Gradecak, poster presented by Z. Zhao at the 12th International Conference on Nitride Semiconductors, Strasbourg, France, Jun 2017.
7. “Efficiency droop mitigation progress in blue and green III-Nitride LEDs,” Hee Jin Kim, Robert Armitage, Tsutomu Ishikawa, Isaac Wildeson, Parijat Deb, Andrew M. Armstrong, Zhibo Zhao, Akshay Singh, Silvija Gradecak and Eric A. Stach, Invited Talk presented by H.J. Kim at the SPIE Optical Engineering + Applications, San Diego, CA, Aug 2017.
8. “Progress on Efficiency Droop Mitigation in Blue and Green LEDs,” Parijat Deb, Costas Dimitropoulos, Hee Jin Kim, Rob Armitage, Tsutomu Ishikawa, Isaac Wildeson, Andrew Armstrong, Zhibo Zhao, Akshay Singh, Silvija Gradečak, Eric Stach, Invited Talk presented by C. Dimitropoulos at the Workshop of Ultra-Precision Processing for Wide Band Gap Semiconductors, 2017 (WUPP-2017), Monterey, CA, Nov 2017.
9. “Cathoduluminescence as an effective probe of carrier transport and deep level defects in InGaN/GaN Quantum Well Heterostructures,” Zhibo Zhao, Akshay Singh, Jordan Chesin, Rob Armitage, Isaac Wildeson, Parijat Deb, Andrew Armstrong, Kim Kisslinger, Eric Stach and Silvija Gradecak, talk presented by Z. Zhao at the MRS Fall 2017 Symposium, Boston MA, Dec 2017.
10. “Impact of Indium distribution in Quantum Wells on efficiency droop in InGaN light emitting diodes,” Sarah Goodman, Akshay Singh, Zhibo Zhao, Dong Su, Kim Kisslinger, Rob Armitage, Isaac Wildeson, Parijat Deb, Eric Stach and Silvija Gradecak, poster presented by S. Goodman at the MRS Fall 2017 Symposium, Boston MA, Dec 2017.
11. “Cathodoluminescence as an Effective Probe of Carrier Transposrt and Deep Level Defects in Droop-Mitigating InGaN/GaN Quantum Well Heterostructures,” Zhibo Zhao, Akshay Singh, Jordan Chesin, Rob Armitage, Isaac Wildeson, Parijat Deb, Andrew Armstrong, Kim Kisslinger, Eric Stach and Silvija Gradecak, manuscript in preparation.

4.3. Inventions and Patent Applications

None